



## RESEARCH PAPER

# Studying microstructure and microstructural changes in plant tissues by advanced diffusion magnetic resonance imaging techniques

Darya Morozov<sup>1,†</sup>, Iris Tal<sup>2,†</sup>, Odelia Pisanty<sup>2</sup>, Eilon Shani<sup>2,\*</sup> and Yoram Cohen<sup>1,\*</sup>

<sup>1</sup> School of Chemistry, The Sackler Faculty of Exact Sciences, and

<sup>2</sup> Department of Molecular Biology and Ecology of Plants, Tel Aviv University, Ramat Aviv, Tel Aviv 66978, Israel

\* Correspondence: [ycohen@post.tau.ac.il](mailto:ycohen@post.tau.ac.il) and [eilonsh@post.tau.ac.il](mailto:eilonsh@post.tau.ac.il)

† These authors contributed equally to this work.

Received 5 January 2017; Editorial decision 10 March 2017; Accepted 12 February 2017

Editor: Chris Hawes, Oxford Brookes University

## Abstract

**As sessile organisms, plants must respond to the environment by adjusting their growth and development. Most of the plant body is formed post-embryonically by continuous activity of apical and lateral meristems. The development of lateral adventitious roots is a complex process, and therefore the development of methods that can visualize, non-invasively, the plant microstructure and organ initiation that occur during growth and development is of paramount importance. In this study, relaxation-based and advanced diffusion magnetic resonance imaging (MRI) methods including diffusion tensor (DTI), *q*-space diffusion imaging (QSI), and double-pulsed-field-gradient (d-PFG) MRI, at 14.1 T, were used to characterize the hypocotyl microstructure and the microstructural changes that occurred during the development of lateral adventitious roots in tomato. Better contrast was observed in relaxation-based MRI using higher in-plane resolution but this also resulted in a significant reduction in the signal-to-noise ratio of the T2-weighted MR images. Diffusion MRI revealed that water diffusion is highly anisotropic in the vascular cylinder. QSI and d-PGSE MRI showed that in the vascular cylinder some of the cells have sizes in the range of 6–10  $\mu\text{m}$ . The MR images captured cell reorganization during adventitious root formation in the periphery of the primary vascular bundles, adjacent to the xylem pole that broke through the cortex and epidermis layers. This study demonstrates that MRI and diffusion MRI methods allow the non-invasive study of microstructural features of plants, and enable microstructural changes associated with adventitious root formation to be followed.**

**Key words:** Adventitious roots, auxin, diffusion MRI (DWI), diffusion tensor imaging (DTI), double-pulsed-field-gradient (d-PGSE) MRI, hypocotyl structure, magnetic resonance imaging (MRI), microstructure, plant development, *q*-space diffusion MRI (QSI), tomato, *Solanum lycopersicum*.

## Introduction

Plant tissues have complex microstructures that are tailored to their function. For example, the branched architecture of a plant's root system is fundamental to its function in supporting plant productivity through both anchorage and uptake of nutrients and water (Van Norman, 2015). The adult plant

root system consists of several types of roots, formed in different developmental contexts. Lateral roots branch from a primary seminal root, formed from the pericycle (Atta *et al.*, 2009), whereas adventitious roots develop on stems or leaves (Bellini *et al.*, 2014). In *Arabidopsis*, adventitious roots in

the hypocotyl initiate from the pericycle cells adjacent to the xylem poles (Boerjan et al., 1995).

Adventitious root formation is a complex process affected by multiple endogenous factors, including hormones and environmental factors (Blakesley, 1994). The plant hormone auxin plays a central role in adventitious root formation (Bellini et al., 2014) as the combined activity of auxin influx and efflux carrier proteins generates auxin maxima and local gradients that inform root patterning (Xu et al., 2005; Petrášek and Friml, 2009). Therefore, auxin is often applied exogenously to promote the development of adventitious roots on stem cuttings (Fogaça and Fett-Neto, 2005).

Lateral and adventitious root formation are well characterized in *Arabidopsis*, but there is limited knowledge on root formation in other species such as tomato. One of the reasons for this is that high-quality data can be obtained from fluorescence microscopy imaging only in relatively thin roots and hypocotyl tissues, such as those of *Arabidopsis*. However, light microscopy, with its relatively low penetration, is of limited value in the study of the thick roots and hypocotyl tissues of most crops (König, 2000; Benediktyová and Nedbal, 2009; Buda et al., 2009). Since live imaging of inner developmental processes of crop plants via light microscopy remains challenging, researchers mostly depend on histology to observe initiation and growth processes that lack temporal resolution. Therefore, we sought to use magnetic resonance imaging (MRI), which has unlimited penetration of plant tissues, to study plant microstructure and microstructural changes associated with root growth and development.

MRI is a powerful technique for studying and gleaning macroscopic and microscopic information in a myriad of chemical and biological systems (Haacke et al., 1999; Stark and Bradley, 1999). MRI was initially derived from nuclear magnetic resonance (NMR) and is a non-invasive technique capable of acquiring data from the entire sample in a non-destructive manner. This tremendous advantage of MRI has opened up a variety of applications in chemical, biomedical, and clinical sciences (Haacke et al., 1999; Stark and Bradley, 1999; Blümich, 2003; Jones, 2010) and in plant research (for reviews see Köckenberger et al., 2004; Van As et al., 2009; Borisjuk et al., 2012; Van As and van Duynhoven, 2013). However, MRI in plant sciences is still far from being a routine tool as it requires, in some cases, dedicated MRI methods and hardware (Van As and van Duynhoven, 2013; Metzner et al., 2015; Nagata et al., 2016). Despite the challenges, in recent years MRI has been used to image the growth of plants in their natural environment (Van As et al., 2009; Borisjuk et al., 2012; Van As and van Duynhoven, 2013), seed and bulb germination and development (Borisjuk et al., 2012), water dynamics of the plant vascular system, and other processes (Van As, 2007; Windt et al., 2009; Sibgatullin et al., 2010; Dean et al., 2014; Gruwel, 2014; Windt and Blümmler, 2015; Nagata et al., 2016; van Dusschoten et al., 2016).

One of the main advantages of MRI is that image contrast depends on the pulse sequence used to collect the measured signal. Indeed, the contrast in MR images can be based on the different type of relaxations and on diffusion, perfusion, susceptibility, magnetization-transfer, chemical exchange

saturation transfer, and more (Haacke et al., 1999; Stark and Bradley, 1999; Blümich, 2003; Jones, 2010). The two commonly used types of MR images are relaxation-based and diffusion-based MR images. In relaxation-based MRI, longitudinal relaxation time (T1), transverse relaxation time (T2), and proton density (PD) MR images can be obtained just by changing the repetition time (TR) and the time-to-echo (TE) parameters. By changing the pulse sequence from spin-echo to gradient-echo the MR image becomes more susceptible to T2\* (Stark and Bradley, 1999). The relaxation-based MRI sequences can be transformed into diffusion-based MRI sequences by adding diffusion-sensitizing gradient pulses as shown in Fig. 1 (Stejskal and Tanner, 1965; Wesbey et al., 1984; Stark and Bradley, 1999; Price, 2009; Jones, 2010).

Diffusion, known also as Brownian motion, results from the random motion of molecules due to internal kinetic energy. The factors that can affect diffusion in a medium are the temperature, the viscosity of the medium, and the hydrodynamic radius of the diffusing particles. For molecules diffusing in a bulk solution, diffusion is Gaussian and isotropic, and the root mean square displacement (*rmsd*) appears equal in all directions and is given by the Einstein equation (Einstein, 1905):

$$rmsd = \sqrt{nDt_d} \quad (1)$$

where *n* is the dimension of motion (2, 4, and 6 for one-, two-, and three-dimensional cases, respectively), *D* is the diffusion coefficient, and *t<sub>d</sub>* is the diffusion time.

The pulsed-field-gradient spin-echo (PGSE) sequence and its imaging version (Fig. 1A) (Stejskal and Tanner, 1965; Wesbey et al., 1984; Price, 2009) are the most commonly used sequences for accurate, non-invasive measurement of diffusion coefficients. In such MR experiments, the signal attenuation, *E*(*q*), for molecular species exhibiting free diffusion is given by Eq. 2 (Stejskal and Tanner, 1965; Price 1997):

$$E(q) = \frac{S(q)}{S(q=0)} = e^{-4\pi^2|q|^2 t_d D} = e^{-(\gamma\delta G)^2 t_d D} = e^{-bD} \quad (2)$$

where the wave vector *q* is defined as:

$$q = (2\pi)^{-1} \delta\gamma G \quad (3)$$

In Eqs 2 and 3,  $\gamma$  is the gyromagnetic ratio, and  $\delta$  and *G* are the pulse-gradient duration and intensity, respectively. When using rectangular gradients, *t<sub>d</sub>* is equal to  $(\Delta - \delta/3)$  where  $\Delta$  is the time between the edges of the two diffusion pulse-gradients. The *b*-value is therefore defined as:

$$b = -4\pi^2 |q|^2 t_d \quad (4)$$

When barriers are introduced into a sample, the diffusing particles may, after a sufficiently long diffusion time, encounter the restricting barriers and consequently the particles will exhibit restricted diffusion. At short diffusion times ( $\Delta < l^2/2D$  where *l* is the size of the compartment), the diffusing particles do not diffuse far enough to probe the barriers

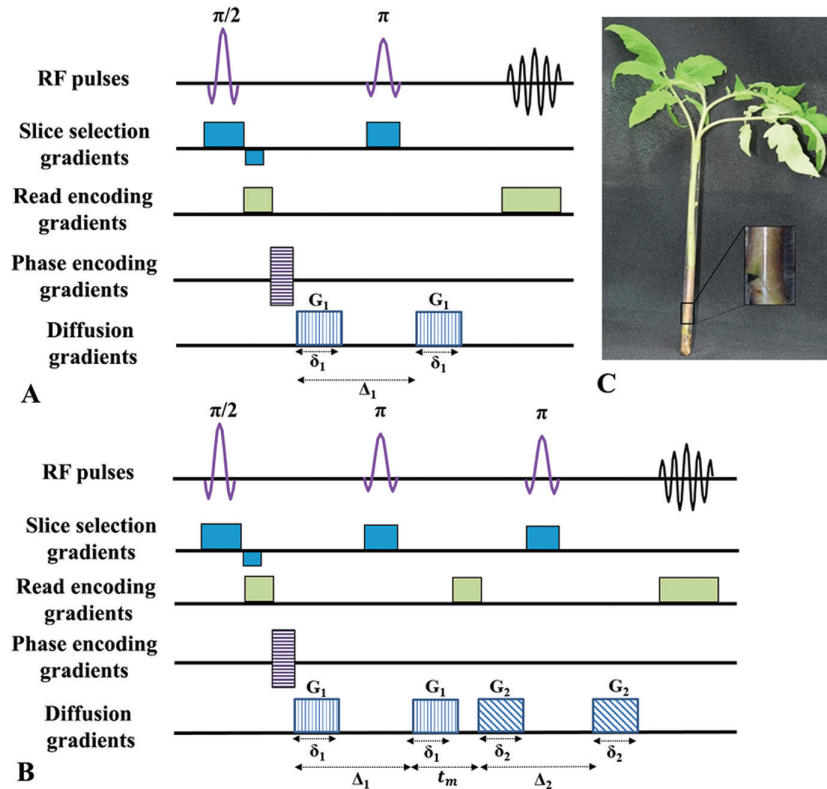


**Fig. 1.** Diffusion MRI pulse sequences. (A) Single PGSE sequence, and (B) a double PGSE sequence. Note that by adding the diffusion sensitizing gradient-pulses (G) the relaxation-based sequence is transformed into the diffusion-based sequence. (C) Image of a horizontally cut whole tomato plant inserted to the NMR tube. Inset in (C) shows a magnification of the nick half-way across the stem to the mid-vasculature. (This figure is available in colour at *JXB* online.)

of the compartment. As a result, the measured diffusion coefficient will be similar to that obtained for the free-diffusing particles. As diffusion time increases and reaches the order of, or surpasses  $l^2/2D$ , an increasing fraction of diffusing particles will feel the effects of the boundary. Hence, the *rmsd* will not scale linearly with the square-root of the diffusion time, resulting in an apparent diffusion coefficient (ADC) (Price, 1997, 2009). At sufficiently long diffusion times, the diffusion of the particles becomes fully restricted by the boundaries and thus the *rmsd* becomes independent of the diffusion time (Price, 1997, 2009; Cohen *et al.*, 2016).

When diffusion is restricted (Tanner and Stejskal, 1968) only in some directions, diffusion is said to be anisotropic (Moseley *et al.*, 1990; Basser, 1995; Price, 1997, 2009; Jones, 2010; Shemesh *et al.*, 2010; Cohen *et al.*, 2016). Therefore, the extracted ADC values will depend significantly on the direction of the measurement, which can be easily controlled in diffusion MR experiments. Diffusion tensor imaging (DTI) is a method in which the diffusion coefficient in Eq. 2 is replaced by a tensor that describes the mobility of molecules in each direction (Basser, 1995; Le Bihan, 1995; Basser and Jones, 2002; Jones, 2010). In order to fully describe a diffusion tensor diffusion experiments should be performed along at least six non-collinear directions (Pierpaoli and Basser, 1996). A  $b_0$  MR image is also required, implying that at least seven MR images are required for DTI. DTI provides several parameters that are a reflection of the sample microstructure in each voxel. One of these parameters is the fractional anisotropy

(FA), which demonstrates the degree of anisotropy in each voxel and varies from 0 (isotropic diffusion) to 1 (fully anisotropic diffusion). DTI also provides the mean diffusivity (MD), which describes the mean motion of the inspected molecules. DTI experiments are used extensively to study central nervous system (CNS) structure and pathologies (Le Bihan, 1995; Johansen-Berg and Behrens, 2009; Jones, 2010; Cohen *et al.*, 2016). In many DTI studies, at least in the CNS, the data has been analysed by assuming Gaussian diffusion and using the well-known Stejskal–Tanner equation (Eq. 2). DTI that has been heavily used in neuroscience and in clinical neurology (Basser and Jones, 2002; Le Bihan, 1995; Johansen-Berg and Behrens, 2009; Jones, 2010; Cohen *et al.*, 2016) has also been used to some extent in plant sciences (Van As *et al.*, 2009; Sibgatullin *et al.*, 2010; Gruwel *et al.*, 2013, 2014; Dean *et al.*, 2014; Gruwel, 2014). For example, Dean *et al.* (2014) used diffusion MRI and DTI to characterize developmental changes in grape berry, while Gruwel (2014) described how this methodology can be used to study plant roots.

However, in many cases of diffusion measurement the signal decay may appear to be non-Gaussian or non-monotonic, implying that the signal decay cannot be analysed using the Stejskal–Tanner equation. In such cases, different approaches are needed to analyse the data. One such approach is the model-free  $q$ -space approach that was originally developed by Callaghan and others to study porous materials and cell sizes (Callaghan *et al.*, 1990, 1991; Cory and Garroway, 1990). We expanded this approach to imaging of

neuronal tissues and organs, to what is now known as  $q$ -space diffusion MRI or QSI (Assaf et al., 2000, 2002; Cohen and Assaf, 2002; Nossin-Manor et al., 2002; Biton et al., 2005, 2007; Bar-Shir et al., 2009; Anaby et al., 2013a, 2013b). QSI involves acquiring a series of diffusion-weighted MR images along a certain direction with increasing  $q$ -values. To analyse the experimental data the signal decay,  $E(q)$ , is Fourier-transformed to afford the displacement probability function  $\bar{P}_s(R, \Delta)$  for each pixel. This analysis is based on the Fourier relationship between  $\bar{P}_s(R, \Delta)$  and  $(q, \Delta)$ :

$$E(q, \Delta) = \int \bar{P}_s(R, \Delta) \exp(i2\pi qR) dR \quad (5)$$

where  $E(q, \Delta)$  represents the signal decay as a function of  $q$ ,  $R$  is the net displacement vector and  $\bar{P}_s(R, \Delta)$  is the displacement probability. The parameters obtained for each pixel in the image are the mean displacement, calculated from the full-width at half height (FWHH) of the displacement distribution profile, and the probability for zero displacement calculated from the height of the displacement profile (Assaf et al., 2000; Cohen and Assaf, 2002). The major limitations of QSI are the requirement for relatively high diffusion weighting (strong gradients), resulting in relatively low signal-to-noise ratios (SNRs), and the need for a relative large number of  $q$ -values, resulting in long acquisition times. Note that QSI has been used to study compartment sizes in stems of asparagus (Lätt et al., 2007).

The double-pulsed-field-gradient (d-PFG) MR methodology (Cory et al., 1990; Mitra, 1995), recently referred to as a double-diffusion encoding (DDE) MR method (Shemesh et al., 2016), is an additional diffusion MRI method for studying and obtaining information on tissue microstructure (Fig. 1B) and has been attracting more interest in recent years (Özarslan, 2009; Shemesh et al., 2010, 2011, 2012a, 2012b; Finsterbusch, 2011; Özarslan et al., 2011; Komlosh et al., 2013). The d-PFG MR method is an extension of the well-known Stejskal–Tanner method and employs two diffusion gradient pairs,  $G_1$  and  $G_2$ , with durations  $\delta_1$  and  $\delta_2$ , respectively. The d-PFG MR sequence contains two diffusion time intervals,  $\Delta_1$  and  $\Delta_2$ , between each gradient pair that may be separated by a mixing time,  $t_m$ . In addition, these two gradient pairs may be applied collinearly (Cory et al., 1990) or with an angle between them (Mitra, 1995), resulting in radial or angular d-PFG MR experiments, respectively.

When an angular d-PFG MR experiment is performed with a zero mixing time and a sufficiently long diffusion time to sense the restriction, the signal will exhibit angular dependency because of the microscopic anisotropy arising from the borders of the confined compartment (Mitra, 1995; Özarslan and Bassar, 2008; Özarslan, 2009; Özarslan et al., 2009). Therefore, zero mixing time angular d-PFG MR experiments have been suggested as an efficient tool for microstructural characterization in systems lacking macroscopic ordering or macroscopic anisotropy (Özarslan and Bassar, 2008; Weber et al., 2009; Shemesh et al., 2010; Finsterbusch, 2011; Lawrenz and Finsterbusch, 2013). Double PFG MRS experiments have been used to study cell sizes in yeast cells and in celery (Özarslan et al., 2011; Shemesh et al., 2012a).

The purpose of the present study was to use relaxation-based MRI and, more importantly, diffusion-based MRI techniques to characterize tomato hypocotyl microstructure and to follow the early stages of the adventitious root initiation process non-invasively.

## Materials and methods

### Plant material

Plants of *Solanum lycopersicum* cv M82, sp<sup>-</sup> were grown in soil in a climate-controlled chamber under long-day conditions (16 h light/8 h dark) at 25 °C.

### Imaging tomato hypocotyls

Five-week-old plants were imaged. Cotyledons and the first four leaves were removed to allow the insertion of the plant with its soil into the NMR tube. The meristem and young developing leaves were not damaged. Plants were inserted into NMR tubes filled with water (Fig. 1C). The tubes were then inserted into the MRI scanner such that the main axis of the plant was aligned along the main magnetic field ( $z$ -axis).

### Imaging adventitious root initiation

Eight-week-old or 5-week-old plants were cut horizontally half-way across the stem to the mid-vasculature, forming a nick. Cotyledons and the first four leaves were removed to allow the insertion of the plant into the NMR tube. The meristem and young developing leaves were not damaged. The tube was then filled with water and leaves were sprayed with solution containing 10  $\mu$ M auxin (IAA) (Duchefa Biochimie 009552) and 0.05% Silwet L-77. Plants were scanned immediately. Between scanning sessions, plants were kept in the growth chamber.

### MRI

All MRI experiments were conducted on a 14.1 T wide-bore NMR scanner (Bruker, Karlsruhe, Germany) equipped with a Great 1 micro-imaging gradient system capable of producing pulsed-field gradients of up to 3 T m<sup>-1</sup> in each direction.

### Experimental parameters for MRI of hypocotyl structure

All MRI experiments examining the hypocotyl structure were conducted with a slice thickness of 1 mm and a field of view (FOV) of 0.45  $\times$  0.45 cm. Three continuous 1-mm slices were acquired with a protocol that included acquisition of T2 maps acquired with a multiple spin-echo Carr–Purcell–Meiboom–Gill-type MR imaging sequence, T1-weighted images, DTI, high  $b$ -value QSI and d-PGSE MR images. The T2 maps were collected with a TR of 3000 ms. The TE was varied between 10–160 ms, with 16 equal steps. The number of averages (NA) was 60. Two T2-weighted images (TE=10 ms and TE=50 ms) were extracted from the T2 map data. The T1-weighted images were collected with TR/TE of 700/15 and NA of 80. The relaxation-based MR images were collected with matrices of 128  $\times$  64 or 256  $\times$  128 (reconstructed to 128  $\times$  128 or 256  $\times$  256), resulting in in-plane spatial resolution of 35  $\times$  70  $\mu$ m<sup>2</sup> or 17  $\times$  35  $\mu$ m<sup>2</sup>, respectively.

All diffusion-based MR images were collected with an in-plane resolution of 35  $\times$  70  $\mu$ m<sup>2</sup>. High  $b$ -value  $q$ -space diffusion MRI (QSI) images (Assaf et al., 2000) were collected using a diffusion-stimulated echo sequence (STE) (Tanner, 1970) acquired in two different directions, perpendicular ( $x$ ) and parallel ( $z$ ) to the plant stem with diffusion time separation ( $\Delta$ ) of 15, 30, and 100 ms and a diffusion gradient duration ( $\delta$ ) of 2 ms. The diffusion gradient strength ( $G$ ) was incremented in 16 equal steps for each direction from 2 to

600 mT m<sup>-1</sup>, resulting in a maximal  $q$ -value of 510 cm<sup>-1</sup> and  $b$ -values of 1263 s mm<sup>-2</sup>, 2607 s mm<sup>-2</sup>, and 8981 s mm<sup>-2</sup> for  $\Delta$ s of 15, 30, and 100 ms, respectively. The QSI data were acquired with TR/TE of 3000/23 and NA of 52, resulting in acquisition time of about 3 h per QSI image.

Diffusion tensor imaging (DTI) experiments were performed using a diffusion spin-echo sequence (SE) with the following parameters: TR/TE=3000/25,  $\Delta/\delta=15/2$  ms. Thirty non-collinear gradient directions were collected with a  $b$ -value of 1263 s mm<sup>-2</sup>, and two additional images were collected with no diffusion weighting ( $b_0$ ). The number of echo planar imaging (EPI) segments (NS) and the NA were set to 4 and 28, respectively, resulting in total acquisition time of about 3 h per DTI data set.

The angular d-PFG MRI sequence used in the present study was based on a d-PGSE sequence (Mitra, 1995) with a finite mixing time ( $t_m$ ) that was integrated into a conventional EPI acquisition scheme (Shemesh *et al.*, 2010, 2011, 2012b). The angular d-PGSE MRI experiments were performed when the  $G_1$  gradient pair was fixed in the  $x$ -direction (perpendicular to main axis of the plant) and the orientation of  $G_2$ , i.e. the second gradient pair, was varied in the  $x$ - $y$  plane. The measurements were conducted with 13 different values of  $q$  between 0° and 360°. The d-PGSE MRI data were collected with the following parameters: TR/TE=3000/40,  $\delta_1=\delta_2=2$  ms,  $\Delta_1=\Delta_2=15$  ms,  $t_m=0$  ms and  $|G_1|=|G_2|=525$  mT m<sup>-1</sup>. These parameters resulted in a  $2q$ -value of 894 cm<sup>-1</sup> and a  $b$ -value of 967 s mm<sup>-2</sup>. The NS and NA values were 4 and 96, respectively, resulting in an acquisition time of about 4 h per d-PGSE MR data set.

#### Experimental parameters for MRI of adventitious root

Additional MRI experiments were conducted with a slice thickness of 1 mm, a FOV of 1 × 1 cm or 0.8 × 0.8 cm, and in-plane resolution of 68 × 68  $\mu$ m<sup>2</sup> or 61 × 61  $\mu$ m<sup>2</sup>, respectively. The MRI protocols for the T2 map images and T1-weighted images were similar to those used for analysis of hypocotyl structure, and only the number of averages was changed. The NA for the T2 maps and T1-weighted MR images were set to 16 and 40, respectively.

DTI experiments were performed with the following parameters: TR/TE of 3000/28 or 3000/23 with in-plane resolutions of 68  $\mu$ m<sup>2</sup> or 61  $\mu$ m<sup>2</sup>, respectively, and  $\Delta/\delta=15/2$  ms. Again, 30 non-collinear gradient directions were collected with a  $b$ -value of 967 s mm<sup>-2</sup> together with two additional  $b_0$  images. The number of EPI segments (NS) and the NA were set to 4 and 10, respectively.

The angular d-PGSE MRI experiments were performed with the following parameters: TR/TE of 3000/41.5 or 3000/40 for in-plane resolution of 68  $\mu$ m<sup>2</sup> or 61  $\mu$ m<sup>2</sup>, respectively,  $\delta_1=\delta_2=2$  ms,  $\Delta_1=\Delta_2=15$  ms,  $t_m=0$  ms and  $|G_1|=|G_2|=525$  mT m<sup>-1</sup>. This resulted in a  $2q$ -value of 894 cm<sup>-1</sup> and a  $b$ -value of 967 s mm<sup>-2</sup>. The NS and NA values were 4 and 26, respectively. The total acquisition time was about 5 h for the entire MRI protocol.

To detect the formation of new roots the plants were scanned at four different time points; immediately and 2, 4, and 7 d after stem cutting and the hormone spray. Since MRI was conducted while plants were unacclimatized to a dark environment, we reduced the NA so that the MRI protocol would be as short as possible. The entire MRI protocol (T1, T2, DTI, and d-PFG MR imaging) lasted about 3.5 h. After undergoing MRI, the plants were transferred to a climate-controlled chamber.

#### Data analysis

To obtain apparent T2 values, the raw data from the T2 mapping experiment were reconstructed to a symmetrical in-plane matrix and analysed using an in-house Matlab program tool. The DTI experiments were analysed using an ExploreDTI tool in Matlab® to produce the FA and the MD maps. The QSI raw data were analysed according to the  $q$ -space approach described previously (Assaf *et al.*, 2000; Cohen and Assaf, 2002). First, the Fourier transformation was performed for each pixel in the image, resulting in a displacement

distribution profile. Next, the displacement value, calculated from the FWHH of the displacement distribution profile, was extracted for each pixel and used to create displacement maps. The d-PGSE MRI data analysis and simulations were based on a method presented previously (Özarslan and Basser, 2008; Özarslan, 2009; Özarslan *et al.*, 2009; Shemesh *et al.*, 2010; Morozov *et al.*, 2015).

#### Histological sections and microscopy

The MRI-scanned hypocotyls were fixed in FAA solution (50% ethanol, 5% acetic acid, and 3.7% formaldehyde) for at least 24 h, and then dehydrated using the tertiary butyl alcohol method (Johansen, 1940). The plant material was embedded in paraffin and cut into 8–12- $\mu$ m thick cross-sections using a Microtome 820 (Spencer) (Johansen, 1940). Following paraffin removal by K-clear (KALTEK - Padova, Italy), the sections were mounted in glycerol and examined by light microscopy.

## Results

### Structural studies of the tomato hypocotyl

#### Conventional relaxation-based MRI

We first used conventional MRI to characterize the morphology of the tomato hypocotyl and to find the optimal in-plane resolution for the diffusion studies that provide the highest spatial resolution along with an adequate SNR at 14.1 T. Figure 2A–C shows the data obtained with an in-plane spatial resolution of 35 × 70  $\mu$ m<sup>2</sup> while Fig. 2D–F shows the same data at an in-plane resolution of 17 × 35  $\mu$ m<sup>2</sup>. Slightly better contrast was observed in Fig. 2D–F as compared to Fig. 2A–C, but the SNRs of the higher-resolution images in Fig. 2D–F were significantly lower than that of the MR images in Fig. 2A–C. These images clearly demonstrate that the higher-resolution MR images have much lower SNRs, especially when the TE was set to 50 ms. Note also that almost no contrast was observed in the T2 maps that were computed (data not shown). In these images it is easy to distinguish between the pith and vascular cylinder areas as they differ in their contrasts. The epidermis and cortex layers with their large compartments are also clearly apparent. Signal intensity in relaxation-based MR images is a reflection of many physical parameters, such as proton density, T1, T2, susceptibility and other factors (Edzes *et al.*, 1998; Van As *et al.*, 2009). At high-spatial-resolution diffusion, susceptibility and other processes may affect the SNR and the contrast observed in long-TE relaxation-based MR images (Edzes *et al.*, 1998; Van As *et al.*, 2009). These MR images, however, do not provide detailed insights into the microstructural characteristics of the plant tissues. Therefore, we decided to revert to diffusion MR imaging, which is known to be more intimately associated with microstructural characteristics of the tissues.

### Diffusion-based MRI of the tomato hypocotyl

#### DTI studies

To examine water diffusion inside the hypocotyl tissues and to get better insights into the structural characteristics of these tissues, we next conducted DTI experiments (Fig. 3).

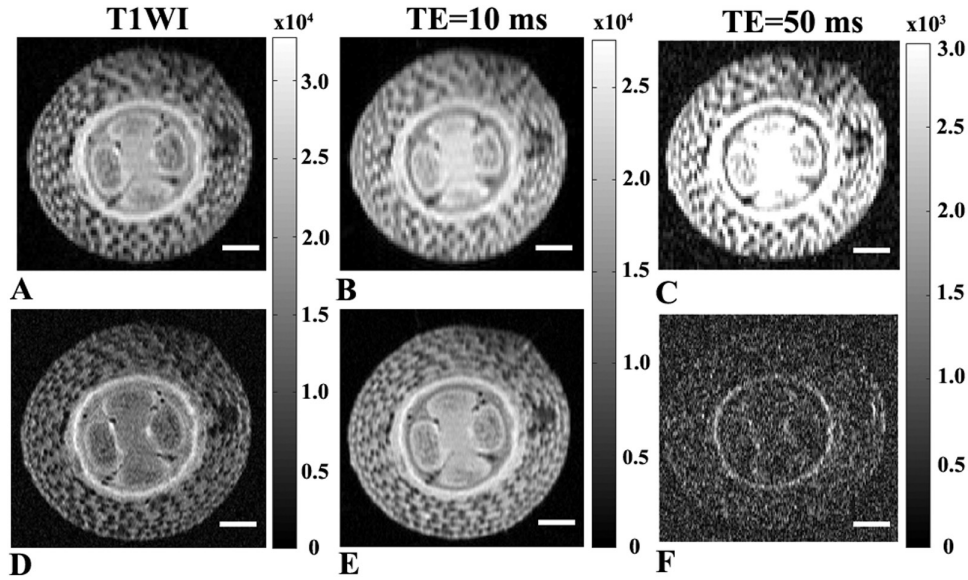


**Fig. 2.** Relaxation-based MR images of tomato hypocotyls. Conventional MR images of 5-week-old tomato hypocotyls obtained with in-plane spatial resolutions of (A–C)  $35 \times 70 \mu\text{m}^2$  and (D–F)  $17 \times 35 \mu\text{m}^2$ . (A, D) T1-weighted images collected with TR/TE of 700/15. (B, E) Short TE T2 MR images (TR/TE=3000/10), (C, F) Long TE T2-weighted images collected with TR/TE of 3000/50. Scale bars are 500  $\mu\text{m}$ .

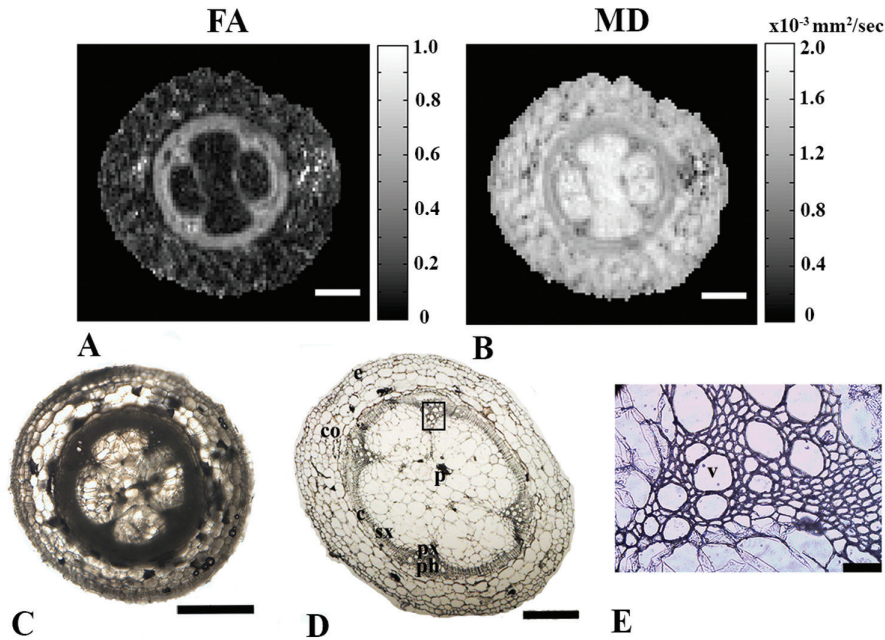


**Fig. 3.** DTI-based MR images of tomato hypocotyls, including correlation with histology. (A) FA and (B) MD maps from DTI ( $b=1263 \text{ s mm}^{-2}$ ,  $\Delta=15 \text{ ms}$ ; scale bars are 500  $\mu\text{m}$ ). (C) Hand-cut- and (D) 12- $\mu\text{m}$  histological cross-sections of 5-week-old tomato hypocotyls (bar are 1 mm and 500  $\mu\text{m}$ , respectively), and (E) enlargement of the vascular bundle depicted on (D) (scale bar is 50  $\mu\text{m}$ ). The abbreviations used for the different regions in (D) and (E) are: px, primary xylem; sx, secondary xylem; ph, phloem; p, pith; c, cambium; co, cortex; e, epidermis; v, vessel.

High FA values were observed in the vascular cylinder region, while low FA values in the range of about 0.2, reminiscent of that observed in grey matter of the CNS (Jones, 2010; Cohen et al., 2016), were observed in other tissues of the tomato hypocotyl (Fig. 3A). This indicates that water diffusion in the phloem and xylem is indeed highly anisotropic. Moreover, low MD values were found in the vascular cylinder, while significantly higher MD values were observed in pith region (Fig. 3B). The FA and MD results shown in Fig. 3A and 3B are consistent with the histological maps obtained from a similar slice of the plant (Fig. 3C, D).

The histological images presented in Fig. 3C and 3D showed that most of the cells in the tomato pith and cortex were around 100  $\mu\text{m}$  in diameter or larger. The cells in the epidermis were twice as small in size as those of the pith and cortex. The only areas where small cells of less than 10  $\mu\text{m}$  were observed were in the vascular region, as shown in Fig. 3E which provides a magnification of the region highlighted in Fig. 3D. To obtain more direct insights into the physical sizes of cells in these areas of the sample it is possible, in principle, to use QSI. QSI generally uses higher diffusion weighting than DTI and has already been used to study neuronal tissue

and other biological cells (Kuchel *et al.*, 1997; Assaf *et al.*, 2000, 2002; Cohen and Assaf, 2002; Lätt *et al.*, 2007; Anaby *et al.*, 2013a, 2013b).

#### QSI studies

QSI studies were performed on the same 5-week-old tomato hypocotyls using a range of diffusion times in two orientations. Figure 4A–C shows displacement maps extracted from QSI studies performed in the  $x$ -direction, perpendicular to the main axis of the plant. These images show that water displacement increased with diffusion time in the epidermis, cortex, and pith cell types. However, the displacement values obtained from the vasculature region varied between 6 and 8  $\mu\text{m}$  when the diffusion time was increased by more than a factor of 6. Figure 4D–F shows QSI displacement maps obtained when the diffusion was measured in the  $z$ -direction, parallel to the main axis of the plant. In this direction, the displacement values in the pith, cortex, and epidermis appeared similar to those obtained from QSI experiments performed in the  $x$ -direction (compare Fig. 4D–F with 4A–C). Interestingly, in the QSI studies performed in the  $z$ -direction no further water restriction was observed in the vascular cylinder region and the displacement maps appeared nearly isotropic across the entire cross-section of the hypocotyl. Thus, in the  $z$ -direction diffusion appears nearly homogenous across the tomato hypocotyl.

#### $d$ -PGSE MRI studies

We next performed angular  $d$ -PGSE MRI studies on 5-week-old tomato hypocotyls with zero mixing time in the  $x$ - $y$  plane (i.e. perpendicular to the main axis of the plant). Figure 5A shows the angle dependency of the normalized signal,  $E(\varphi)$ , of the hypocotyl. Only the vascular cylinder cells showed a bell-shaped signal dependency, and the signal in these areas was

found to increase to from  $0^\circ$  to  $180^\circ$  followed by a decrease to  $360^\circ$  (Fig. 5A). Interestingly, no angular dependencies were observed in other hypocotyl regions. Figure 5B and 5C present signal profiles and a  $k$ -means clustering segmentation of the different tissues of the hypocotyl into six different clusters. The six clusters identified were found to have very different angle dependencies of  $E(\varphi)$ . Clusters 4–6 showed nearly no angle dependencies of  $E(\varphi)$ , reminiscent of free diffusion. However, clusters 1–3 showed the expected bell-shaped signal dependency (Fig. 5C). Figure 5D shows the normalized  $E(\varphi)$  profiles along with the respective simulations for the three clusters originating from the vascular cylinder region (xylem and phloem areas). Very good agreement was found between the simulations and the experimental data. Based on these analyses, cell diameters in the range of 8 to 10  $\mu\text{m}$  were extracted (Fig. 5D). These sizes are in good agreement with the cell diameters in this area as seen using histology (Fig. 3E).

#### MRI of adventitious root formation

To promote adventive root formation, we generated artificial auxin maxima at the scanning position. Eight-week-old tomato plants were treated with a solution containing 10  $\mu\text{M}$  auxin (sprayed on developing leaf primordia) and the hypocotyls were cut horizontally half-way across the stem (1.5 mm), generating a nick up to the mid-vasculature and resulting in accumulation of auxin above the site of the cut. The tomato plants were immersed whole into water to allow the development of adventitious roots.

The MR images presented in Fig. 6 were collected 24 h after generation of the artificial auxin maxima. These images show that the new roots initiate from the vascular bundle periphery/pericycle region and break their way out through

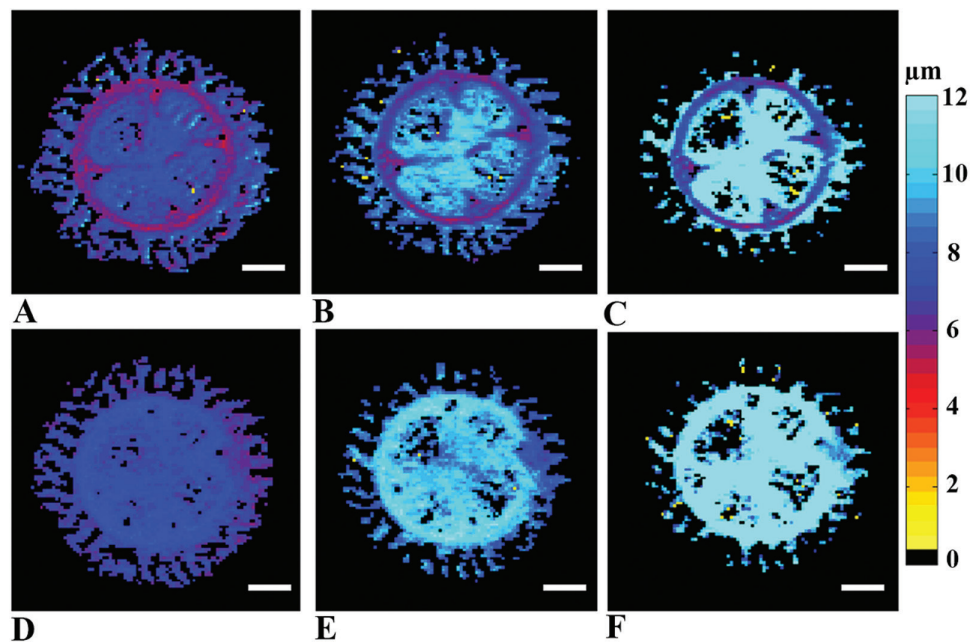


**Fig. 4.** QSI-based images of tomato hypocotyls. Displacement maps of 5-week-old tomato hypocotyls extracted from high  $b$ -value QSI experiments performed in (A–C) the  $x$ -direction and (D–F) the  $z$ -direction, with three different diffusion times of (A, D) 15 ms, (B, E) 30 ms, and (C, F) 100 ms. Scale bars are 500  $\mu\text{m}$ . (This figure is available in colour at *JXB* online.)

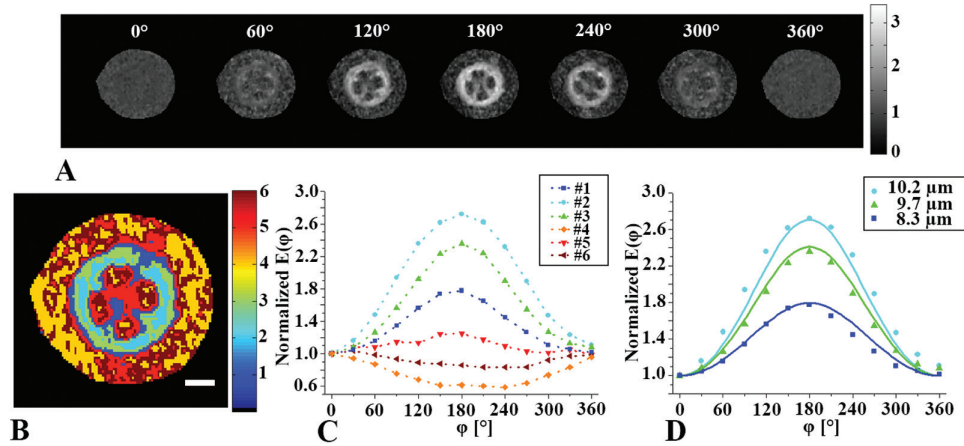


**Fig. 5.** d-PGSE MRI analyses of tomato hypocotyls. (A) Raw data from the angular d-PGSE MRI experiment with zero mixing time conducted on 5-week-old tomato hypocotyls when  $\varphi$  was rotated in the  $x$ - $y$  plane (i.e. perpendicular to the main axis of the plant). (B)  $k$ -means clustering analysis of the data presented in (A); The scale bar is 500  $\mu\text{m}$ . (C) Normalized  $E(\varphi)$  profiles of the clusters shown in (B). (D) Normalized  $E(\varphi)$  profiles obtained from clusters in the vascular bundle region (symbols). Simulated curves are shown as lines for the indicated sizes. (This figure is available in colour at *JXB* online.)

the cortex and epidermis cells. This is visible on the apparent T2-map and the T1-weighted MR image (Fig. 6A and B). However, more significant contrast between the developing adventitious roots and the cortex tissues is apparent on the T1-weighted MR image. Note that in this case the in-plane resolution was significantly lower than in Figs 2–5, resulting in higher SNR. Figure 6C and 6D show that, at this developmental stage, the FA and MD values obtained for adventitious roots were more similar to those of the vascular bundles (xylem and phloem areas) than to cortex and epidermis. Moreover, the bundle region around the initiation site of the adventitious root seems to be wider than in other areas of the vascular bundle and secondary xylem perimeter. Figure 6E also shows the zero-mixing time d-PGSE MR image for  $\varphi$  of 180° collected on the same plant. In this MR image, regions consisting of relatively small cells were observed mostly in the vascular cylinder, namely the primary bundles, cambium, phloem, and secondary xylem (see also Fig. 5), and seemingly in some areas of the adventitious roots (Fig. 6E, arrows). Figure 6F presents the histological section obtained from the same tomato hypocotyl at a similar development stage but at slightly different plane. In this stage of development, some of the cells of the initiating adventitious root were smaller than other cells in the cortex but appeared larger compared to the vascular cylinder cells. This may be the reason why the adventitious root cells appeared less intense in the FA map obtained from DTI (Fig. 6C) and in the zero-mixing time d-PGSE MR image (Fig. 6E).

Next, we followed the time-course of the formation of adventitious root by MR imaging. The base of hypocotyls of 5-week-old tomato plants were cut to form a nick to the mid-vasculature. Plants were then inserted into NMR tubes filled with water. The MRI protocol was shorter than that used to collect the data shown in Fig. 6 in order to minimize the effect of the MRI measurement on development, resulting in somewhat lower SNRs in the different MR images collected. During the first two days after nicking, no significant tissue changes were observed under these

imaging conditions (Fig. 7). The formation of new adventitious roots, however, was apparent at day 4 after induction of adventitious root formation. Root formation was observed in all the MR images collected at this time point. These images and those collected at day 7 showed that the adventitious root that were formed initiated from the primary vascular bundle periphery region (peri-vasculature parenchyma cells/pericycle) and then developed through the cortex. Interestingly, cell proliferation was observed at days 4 and 7; however, some tissue reorganization was observed even at day 2. These MR data indicate that some structural changes occurred in the vasculature areas at the early stages of adventitious root formation.

## Discussion

In this work, we have shown that MRI, and more specifically advanced diffusion MRI, is able to characterize some facets of hypocotyl microstructure and can provide significant insights into the process of adventitious root formation in a non-invasive manner.

First, we conducted relaxation-based MRI by collecting T1-weighted and T2-weighted MR images at two different in-plane resolutions (Fig. 2). The MR images collected with higher in-plane resolution showed, as expected, slightly more detailed structural information for the hypocotyl tissue, although with low SNRs. The cortex cells were easily visualized at both in-plane resolutions, and were observed to be polygonal and closely packed. The sizes of the vascular bundle cells could not be visualized directly by the T1-weighted and the T2-weighted MR images at the spatial resolutions used in this study, since many of these cells are significantly smaller than cortex cells, having diameters in the range of 8–12  $\mu\text{m}$  (Fig. 4D). The cells of the pith region are similar in diameter or even larger than the cells in the cortex, but these cells were not clearly apparent on the T1-weighted and T2-weighted MR images, and consequently the pith region appears hyper-intense compared to the vascular bundle area.



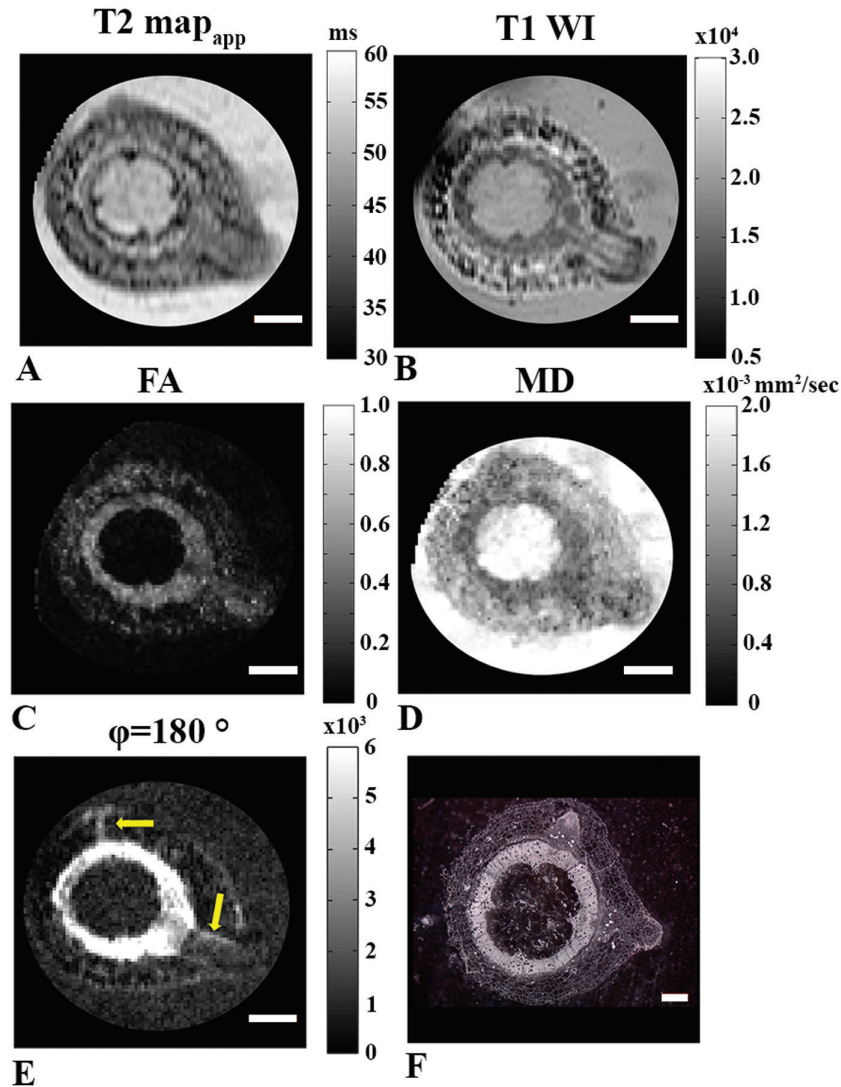


**Fig. 6.** MR images obtained 24 h after adventitious root formation in 8-week-old plants (in-plane resolution of  $68 \mu\text{m}^2$ ). (A) Apparent T2 map (TR/TE=3000/10–160). (B) T1-weighted image (TR/TE=700/15). (C) FA image. (D) MD image from DTI ( $b=1263 \text{ s mm}^{-2}$ ,  $\Delta=15 \text{ ms}$ ). (E) d-PGSE MR image for  $\varphi$  of  $180^\circ$ . Regions of small cells are indicated by the arrows. Scale bars in (A–E) are 1 mm. (F) Histological section at a slightly different location of the same hypocotyl; the scale bar is  $500 \mu\text{m}$ .

Water molecules have relatively long T1 and T2 values, lipids in membranes have short T1 and T2 values, and macromolecules generally have long T1 and short T2 values. Therefore, it is not surprising that these relaxation properties are used as contrast in MRI. We found a high signal inside the cortex cells but, as expected, less signal between the cells since the membranes have relatively lower water content and may have short T2 values. Moreover, the T2 MR maps computed (data not showed) had low SNRs, especially those with the higher in-plane resolution. The images presented in Fig. 2C and 2F indicate that the contrast and even the SNR in the relaxation-based MR images at high resolution and long TE are to some extent also affected by susceptibility, diffusion, and other effects related to the MR acquisition scheme, such as the high read-out gradients used (Edzes *et al.*, 1998; Van As *et al.*, 2009). Therefore, the apparent T2 values extracted from such MR experiments are usually smaller than the intrinsic ones. These effects become even larger at high magnetic fields and at high in-plane resolution of the kind used in the present

study. The low SNRs observed in the long TE T2-weighted MR images with the higher resolution led us to prefer the use of the lower in-plane resolution in the diffusion MR images we collected next.

To obtain microstructural information on the hypocotyl tissues we collected advanced diffusion MRI data. First, we collected DTI data as shown in Fig. 3. High FA and low MD values were extracted from DTI in the vascular cylinder region as compared to other regions of the hypocotyl. These results imply that water diffusion in these bundles is anisotropic and can be probed with moderate diffusion time. This anisotropy probably originates from the highly packed, coherently organized, elongated cells in these areas. Interestingly, the MD values in pith region were found to be high and reminiscent of free water, indicating that water molecules inside the pith region exhibit mostly free diffusion under the experimental conditions used. The DTI results obtained were consistent with the histological image obtained from a similar slice of the plant, indicating that DTI indices could potentially be

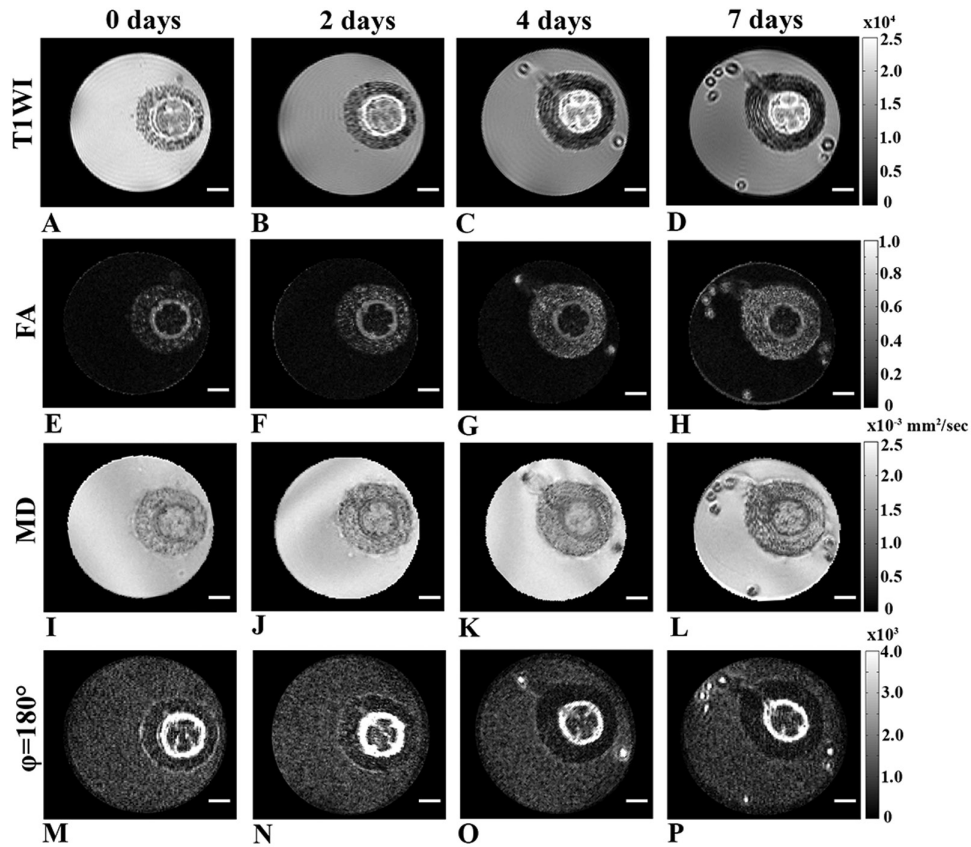


**Fig. 7.** Time-course of adventitious root formation in 5-week-old plants by live MRI imaging (in-plane resolution of  $61 \mu\text{m}^2$ ). (A–D) T1-weighted images, (E–H) FA images, and (I–L) MD maps obtained from DTI. (M–P) Zero mixing time d-PGSE MR images for  $\varphi$  of  $180^\circ$  map. All scale bars are 1 mm.

used as biomarkers for hypocotyl macroscopic organization. However, DTI, which is based on the assumption that water diffusion is Gaussian, is less suitable to describe diffusion in confined geometries and to provide specific, quantitative microstructural information. To obtain such information we performed QSI experiments with different diffusion times and in different directions of the hypocotyl (Fig. 4). When the QSI experiments, collected with a stimulated echo-based diffusion sequence, were conducted along the  $x$ -direction (i.e. perpendicular to the main axis of the hypocotyl) an increase in the diffusion time resulted in larger water displacement both in cortex and pith areas. In the vascular bundle regions, however, only a very small increase in the mean displacement was observed with the increase in diffusion time. The displacement values obtained from the vascular regions remained almost without change and varied between  $6\text{--}8 \mu\text{m}$  when the diffusion time was varied from 15 to 100 ms. This indicates that in the vascular bundle regions, water diffusion in the direction perpendicular to the main hypocotyl axis is quite restricted. The fact that some increase in the mean displacement and in the extracted sizes was observed when the diffusion time was increased suggests that the membranes are not completely impermeable (Sibgatullin et al., 2010). Note that to probe water restriction in cortex and pith cells, the size of which are  $100 \mu\text{m}$  or more, extremely long diffusion times in the region of 2.5 s should be used. These diffusion times are impractical and are much longer than those applied in the present study since we have used a 14.1-T instrument, where

susceptibility effects are significant and apparent T2s are relatively short. At a lower magnetic field (3 T), however, it is possible to perform diffusion measurements with diffusion times of up to 1 s (Sibgatullin et al., 2010). When QSI experiments were conducted parallel to the main axis of the plant, very similar displacement values were obtained for all regions including the vascular bundles at all diffusion times, resulting in relatively smooth displacement maps. Moreover, in this direction the displacement increased nearly linearly with the square-root of the diffusion time, suggesting that water diffusion is essentially free parallel to the main axis of the plant. These results indicate that the vascular bundle region consists mainly of coherently organized and highly packed cells with cylindrical geometry. In contrast, the QSI data seem to suggest that most cells of the cortex and pith are relatively large and probably spherical.

To further characterize the hypocotyl microstructure, angular d-PGSE MRI experiments with zero mixing times were conducted in the  $x$ - $y$  plane, perpendicular to the main axis of the same plant (Fig. 5). The raw images obtained showed a bell-shaped signal dependency only for signals originating from the vascular bundles. The signal of the bundle cells increased from  $0^\circ$  to  $180^\circ$  and then decreased from  $180^\circ$  to  $360^\circ$ . Interestingly, no angular dependency was obtained for signals originating from other plant regions. This is in accordance with the results from DTI, QSI, and histology, which showed that the cells in the cortex and the pith tissues are large, making it impossible, with the experimental conditions used in the present study, to

probe restriction of water diffusion there. The clustering analysis showed different angular dependencies in different cells in the vascular cylinder, suggesting that angular d-PGSE MRI has the ability to differentiate between different areas and, more importantly, to segment the vascular bundle into regions based on cell size. Simulations of the d-PFG MRI experimental signals were found to be in good agreement with the experimental data and cell sizes in the range of 8–10  $\mu\text{m}$  were extracted. It is interesting to note that the cells in the vascular cylinder are organized into three circular clusters. On average, cells in the interior of the vascular bundles were the largest, and the smaller cells were observed in the outer periphery of the vascular cylinder. These observations are consistent with the histology results presented in Fig. 3D.

As MRI can provide structural information and advanced diffusion MRI can reveal microstructural features in plant tissues non-invasively, we sought to visualize adventitious root initiation using these MRI techniques (Fig. 6). This was an even more difficult task as we had to use plants with smaller hypocotyl cross-sections, and because the plants had to be immersed in water when we collected the MRI data. The latter resulted in a high background signal in some of the MR images. The MRI data collected following nicking of the hypocotyl to initiate adventive root formation showed that the new roots emerged from the primary vascular bundles and out through the cortex. Low FA and high MD values were found in the pith region of the plant and, interestingly, the FA and MD values of initiating adventitious roots were more similar to those of vascular bundle cells, indicating that the newly formed cells were relatively small or densely packed. Moreover, we observed that the vascular bundles thickened where the adventitious roots started to occur, suggestive of high levels of cellular proliferation in the region of root initiation. In addition, both the FA from DTI and d-PGSE MR ( $\varphi=180^\circ$ ) images seemed to indicate that some reorganization occurred in the vascular bundles where the adventitious roots developed (Fig. 6C and 6E). Our data indicate more isotropic diffusion in the area of root development, which may originate from the formation of more isotropic or larger cells. Histological images obtained from similar tissue were found to be in good agreement with the MRI findings. Histology and MRI suggested that some of the cells in the initiating adventitious root were somewhat smaller than those of cortex, but probably larger than the cells in the vascular cylinder.

After characterizing the structural changes associated with adventitious root formation, we followed the time-course of this process by live MRI imaging (Fig. 7). This was an even more challenging task since we had to shorten the MRI protocol, which resulted in lower SNRs in the obtained images. The formation of new adventitious roots was detected in all MR images after 4 d. The roots initiated from the vascular bundle regions, developed through the cortex, and broke out through the hypocotyl epidermis. Interestingly, cell proliferation that resulted in structural changes was not observed after 2 d (Fig. 7). The time-course of the development of the adventitious roots was slower inside than outside the magnet. This may be the result of the stress imposed on the plant in the magnetic field and, more importantly, due to the fact that

our MRI measurements were performed in a high-resolution MRI scanner where the plants were in the dark. For plants that were not in the magnet, root development was found to be faster. These observations show that the high-field MRI scanner used in the present study, which provided a wealth of structural information and some microstructural features of the plant tissues, is less suitable for studying time-courses of plant physiology since the measurement itself seems to affect to some extent the time-course of the natural development of the roots. A partial solution would be to provide illumination within the magnet or to use a dedicated MRI system with a magnet that allows performing such study in the natural environment. Indeed, in recent years several such MRI systems, most of which have relatively low fields, have been described in the literature (Van As, 2007; Nagata *et al.*, 2016). However, these instruments generally have lower sensitivity and homogeneity compared with the MRI scanner used here, making it more difficult to implement advanced MRI techniques.

There are additional methods for plant visualization, such as micro-CT, cryo-sem (Choat *et al.*, 2015; Umebayashi *et al.*, 2016), or positron emission tomography (PET) (Converse *et al.*, 2015). However, MRI has several important advantages, the main one being that, compared to other imaging methods, MRI is a true multi-parametric method where the image contrast can provide information on a range of tissue characteristics, from proton density and relaxation, through to susceptibility, diffusion, and flow. In addition, MRI has an unlimited penetration to plant tissues, uses safe RF pulses, and is less invasive and more environmentally friendly. We therefore anticipate that MRI will contribute more to plant research in the future.

## Conclusions

In this study, we show that multi-parametric MRI methods and advanced diffusion MRI methods may provide important information on plant tissues. Diffusion MRI techniques provide powerful tools for characterizing, with great detail and non-invasively, structure and microstructural features of the plant tissues as well as developmental processes in live plants. We show that diffusion MRI techniques, such as DTI, QSI, and d-PGSE, provide unique tools to study the macro- and microscopic organization of the plant and, after proper modelling, allow the estimation of the sizes of some of the plant cells with high accuracy, thus providing a novel dynamic spatiotemporal ‘virtual histology’. The main advantages of MRI are its non-invasiveness and the fact that many different images can be acquired, each sensitive to different sets of physical parameters reflecting different physiological or biological process. Therefore, we believe that multi-parametric MRI and diffusion MRI have the potential for following complex biological processes in plants.

## Acknowledgments

We thank Roni Aloni (TAU) and Amnon Schwartz (HUJI) for critical reading of the manuscript. This work was supported by grants from the Israeli Ministry of Agriculture (13-01-0010) to ES.

## References

- Anaby D, Duncan ID, Smith CM, Cohen Y.** 2013a. *q*-Space diffusion MRI (QSI) of the disease progression in the spinal cords of the Long Evans shaker: diffusion time and apparent anisotropy. *NMR in Biomedicine* **26**, 1879–1886.
- Anaby D, Duncan ID, Smith CM, Cohen Y.** 2013b. White matter maturation in the brains of Long Evans shaker myelin mutant rats by *ex-vivo* QSI and DTI. *Magnetic Resonance Imaging* **31**, 1097–1104.
- Assaf Y, Ben-Bashat D, Chapman J, et al.** 2002. High *b*-value *q*-space analyzed diffusion-weighted MRI: application to multiple sclerosis. *Magnetic Resonance in Medicine* **47**, 115–126.
- Assaf Y, Mayk A, Cohen Y.** 2000. Displacement imaging of spinal cord using *q*-space diffusion-weighted MRI. *Magnetic Resonance in Medicine* **44**, 713–722.
- Atta R, Laurens L, Boucheron-Dubuisson E, Guivarc'h A, Carnero E, Giraudat-Pautot V, Rech P, Chriqui D.** 2009. Pluripotency of Arabidopsis xylem pericycle underlies shoot regeneration from root and hypocotyl explants grown *in vitro*. *The Plant Journal* **57**, 626–644.
- Bar-Shir A, Duncan ID, Cohen Y.** 2009. QSI and DTI of excised brains of the myelin-deficient rat. *Neuroimage* **48**, 109–116.
- Basser PJ.** 1995. Inferring microstructural features and the physiological state of tissues from diffusion-weighted images. *NMR in Biomedicine* **8**, 333–344.
- Basser PJ, Jones DK.** 2002. Diffusion-tensor MRI: theory, experimental design and data analysis – a technical review. *NMR in Biomedicine* **15**, 456–467.
- Bellini C, Pacurar DI, Perrone I.** 2014. Adventitious roots and lateral roots: similarities and differences. *Annual Review of Plant Biology* **65**, 639–666.
- Benediktyová Z, Nedbal L.** 2009. Imaging of multi-color fluorescence emission from leaf tissues. *Photosynthesis Research* **102**, 169–175.
- Biton IE, Duncan ID, Cohen Y.** 2007. *q*-Space diffusion of myelin-deficient spinal cords. *Magnetic Resonance in Medicine* **58**, 993–1000.
- Biton IE, Mayk A, Kidron D, Assaf Y, Cohen Y.** 2005. Improved detectability of experimental allergic encephalomyelitis in excised swine spinal cords by high *b*-value *q*-space DWI. *Experimental Neurology* **195**, 437–446.
- Blakesley D.** 1994. Auxin metabolism and adventitious root initiation. In: **Davis TD, Haissig BE**, eds. *Biology of adventitious root formation*. New York: Springer, 143–154.
- Blümich B.** 2003. *NMR imaging of materials*. Oxford: Clarendon Press.
- Boerjan W, Cervera MT, Delarue M, et al.** 1995. Superroot, a recessive mutation in Arabidopsis, confers auxin overproduction. *The Plant Cell* **7**, 1405–1419.
- Borisjuk L, Rolletschek H, Neuberger T.** 2012. Surveying the plant's world by magnetic resonance imaging. *The Plant Journal* **70**, 129–146.
- Buda GJ, Isaacson T, Matas AJ, Paolillo DJ, Rose JK.** 2009. Three-dimensional imaging of plant cuticle architecture using confocal scanning laser microscopy. *The Plant Journal* **60**, 378–385.
- Callaghan PT, Coy A, MacGowan D, Packer KJ, Zelaya FO.** 1991. Diffraction-like effects in NMR diffusion studies of fluids in porous solids. *Nature* **351**, 467–439.
- Callaghan PT, MacGowan D, Packer K, Zelaya F.** 1990. High-resolution *q*-space imaging in porous structures. *Journal of Magnetic Resonance* **90**, 177–182.
- Choat B, Brodersen CR, McElrone AJ.** 2015. Synchrotron X-ray microtomography of xylem embolism in *Sequoia sempervirens* saplings during cycles of drought and recovery. *New Phytologist* **205**, 1095–1105.
- Cohen Y, Anaby D, Morozov D.** 2016. Diffusion MRI of the spinal cord: from structural studies to pathology. *NMR in Biomedicine* **30**, e3592.
- Cohen Y, Assaf Y.** 2002. High *b*-value *q*-space analyzed diffusion-weighted MRS and MRI in neuronal tissues – a technical review. *NMR in Biomedicine* **15**, 516–542.
- Converse AK, Ahlers EO, Bryan TW, Williams PH, Barnhart TE, Engle JW, Nickles RJ, DeJesus OT.** 2015. Positron emission tomography (PET) of radiotracer uptake and distribution in living plants: methodological aspects. *Journal of Radioanalytical and Nuclear Chemistry* **297**, 241–246.
- Cory DG, Garroway AN.** 1990. Measurement of translational displacement probabilities by NMR: an indicator of compartmentation. *Magnetic Resonance in Medicine* **14**, 435–444.
- Cory DG, Garroway AN, Miller JB.** 1990. Applications of spin transport as a probe of local geometry. *Polymer Preprints* **3**, 149–150.
- Dean RJ, Stait-Gardner T, Clarke SJ, Rogiers SY, Bobek G, Price WS.** 2014. Use of diffusion magnetic resonance imaging to correlate the developmental changes in grape berry tissue structure with water diffusion patterns. *Plant Methods* **10**, 35.
- Edzes HT, van Dusschoten D, Van As H.** 1998. Quantitative T2 imaging of plant tissues by means of multi-echo MRI microscopy. *Magnetic Resonance Imaging* **16**, 185–196.
- Einstein A.** 1905. On the motion required by molecular kinetic theory of heat of small particles suspended in a stationary liquid. *Annalen der Physik* **17**, 549–560.
- Finsterbusch J.** 2011. Multiple-wave-vector diffusion-weighted NMR. *Annual Reports on NMR Spectroscopy* **72**, 225–299.
- Fogaça CM, Fett-Neto AG.** 2005. Role of auxin and its modulators in the adventitious rooting of *Eucalyptus* species differing in recalcitrance. *Plant Growth Regulation* **45**, 1–10.
- Gruwel MLH.** 2014. *In situ* magnetic resonance imaging of plant roots. *Vadose Zone Journal* **13**, 3.
- Gruwel MLH, Latta P, Sbotto-Frankenstein U, Gervai P.** 2013. Visualization of water transport pathways in plants using diffusion tensor imaging. *Progress in Electromagnetics Research C* **35**, 73–82.
- Haacke EM, Brown RW, Thompson MR, Venkatesan R.** 1999. *Magnetic resonance imaging: physical principles and sequence design*. New York: Wiley-Liss.
- Johansen DA.** 1940. *Plant microtechnique*. New York and London: McGraw-Hill Book Company.
- Jones DK.** 2010. *Diffusion MRI: theory, methods, and applications*. New York: Oxford University Press.
- Johansen-Berg H, Behrens TEJ.** 2009. *Diffusion MRI: From quantitative measurements to in vivo neuroanatomy*. Amsterdam: Academic Press.
- Köckenberger W, De Panfilis C, Santoro D, Dahiya P, Rawsthorne S.** 2004. High resolution NMR microscopy of plants and fungi. *Journal of Microscopy* **214**, 182–189.
- Komlos ME, Özarslan E, Lizak MJ, Horkayne-Szakaly I, Freidlin RZ, Horkay F, Basser PJ.** 2013. Mapping average axon diameters in porcine spinal cord white matter and rat corpus callosum using d-PFG MRI. *Neuroimage* **78**, 210–216.
- König K.** 2000. Multiphoton microscopy in life sciences. *Journal of Microscopy* **200**, 83–104.
- Kuchel PW, Coy A, Stilbs P.** 1997. NMR “diffusion-diffraction” of water revealing alignment of erythrocytes in a magnetic field and their dimensions and membrane transport characteristics. *Magnetic Resonance in Medicine* **37**, 637–643.
- Lätt J, Nilsson M, Rydhög A, Wirestam R, Ståhlberg F, Brockstedt S.** 2007. Effects of restricted diffusion in a biological phantom: a *q*-space diffusion MRI study of asparagus stems at a 3T clinical scanner. *Magnetic Resonance Materials in Physics, Biology and Medicine* **20**, 213–222.
- Lawrenz M, Finsterbusch J.** 2013. Double-wave-vector diffusion-weighted imaging reveals microscopic diffusion anisotropy in the living human brain. *Magnetic Resonance in Medicine* **69**, 1072–1082.
- Le Bihan D.** 1995. *Magnetic resonance imaging of diffusion and perfusion: applications to functional imaging*. New York: Lippincott-Raven Press.
- Metzner R, Eggert A, van Dusschoten D, Pflugfelder D, Gerth S, Schurr U, Uhlmann N, Jahnke S.** 2015. Direct comparison of MRI and X-ray CT technologies for 3D imaging of root systems in soil: potential and challenges for root trait quantification. *Plant Methods* **11**, 17.
- Mitra PP.** 1995. Multiple wave-vector extensions of the NMR pulsed-field-gradient spin-echo diffusion measurement. *Physical Review. B* **51**, 15074–15078.
- Morozov D, Bar L, Sochen N, Cohen Y.** 2015. Microstructural information from angular double-pulsed-field gradient NMR: from model systems to fixed nerves. *Magnetic Resonance in Medicine* **74**, 25–32.
- Moseley ME, Cohen Y, Kucharczyk J, Mintorovitch J, Asgari HS, Wendland MF, Tsuruda J, Norman D.** 1990. Diffusion-weighted MR

imaging of anisotropic water diffusion in cat central nervous system. *Radiology* **176**, 439–445.

**Nagata A, Kose K, Terada Y.** 2016. Development of an outdoor MRI system for measuring flow in a living tree. *Journal of Magnetic Resonance* **265**, 129–138.

**Nossin-Manor R, Duvdevani R, Cohen Y.** 2002. *q*-Space high *b* value diffusion MRI of hemi-crush in rat spinal cord: evidence for spontaneous regeneration. *Magnetic Resonance Imaging* **20**, 231–241.

**Özarslan E.** 2009. Compartment shape anisotropy (CSA) revealed by double pulsed field gradient MR. *Journal of Magnetic Resonance* **199**, 56–67.

**Özarslan E, Bassar PJ.** 2008. Microscopic anisotropy revealed by NMR double pulsed field gradient experiments with arbitrary timing parameters. *The Journal of Chemical Physics* **128**, 154511.

**Özarslan E, Komlosh ME, Lizak MJ, Horkay F, Bassar PJ.** 2011. Double pulsed field gradient (double-PFG) MR imaging (MRI) as a means to measure the size of plant cells. *Magnetic Resonance in Chemistry* **49**, S79–S84.

**Özarslan E, Shemesh N, Bassar PJ.** 2009. A general framework to quantify the effect of restricted diffusion on the NMR signal with applications to double pulsed field gradient NMR experiments. *The Journal of Chemical Physics* **130**, 104702.

**Petrásek J, Friml J.** 2009. Auxin transport routes in plant development. *Development* **136**, 2675–2688.

**Pierpaoli C, Bassar PJ.** 1996. Toward a quantitative assessment of diffusion anisotropy. *Magnetic Resonance in Medicine* **36**, 893–906.

**Price WS.** 1997. Pulsed-field gradient nuclear magnetic resonance as a tool for studying translational diffusion: Part 1. Basic theory. *Concepts in Magnetic Resonance* **9**, 299–336.

**Price WS.** 2009. *NMR studies of translational motion: principles and applications*. Cambridge: Cambridge University Press.

**Shemesh N, Adiri T, Cohen Y.** 2011. Probing microscopic architecture of opaque heterogeneous systems using double-pulsed-field-gradient NMR. *Journal of the American Chemical Society* **133**, 6028–6035.

**Shemesh N, Barazany D, Sadan O, et al.** 2012a. Mapping apparent eccentricity and residual ensemble anisotropy in the gray matter using angular double-pulsed-field-gradient MRI. *Magnetic Resonance in Medicine* **68**, 794–806.

**Shemesh N, Jespersen SN, Alexander DC, et al.** 2016. Conventions and nomenclature for double diffusion encoding NMR and MRI. *Magnetic Resonance in Medicine* **75**, 82–87.

**Shemesh N, Özarslan E, Bassar PJ, Cohen Y.** 2012b. Accurate noninvasive measurement of cell size and compartment shape anisotropy in yeast cells using double-pulsed field gradient MR. *NMR in Biomedicine* **25**, 236–246.

**Shemesh N, Özarslan E, Komlosh ME, Bassar PJ, Cohen Y.** 2010. From single-pulsed field gradient to double-pulsed field gradient MR:

gleaning new microstructural information and developing new forms of contrast in MRI. *NMR in Biomedicine* **23**, 757–780.

**Sibgatullin TA, Vergeldt FJ, Gerkema E, Van As H.** 2010. Quantitative permeability imaging of plant tissues. *European Biophysics Journal* **39**, 699–710.

**Stark DD, Bradley WG Jr.** 1999. *Magnetic resonance imaging*. St.Louis: CV Mosby and Co.

**Stejskal EO, Tanner JE.** 1965. Spin diffusion measurements: spin echoes in the presence of a time-dependent field gradient. *The Journal of Chemical Physics* **42**, 288–292.

**Tanner JE.** 1970. Use of stimulated echo in NMR diffusion studies. *The Journal of Chemical Physics* **52**, 2523–2528.

**Tanner JE, Stejskal EO.** 1968. Restricted self-diffusion of protons in colloidal systems by the pulsed-gradient spin echo method. *The Journal of Chemical Physics* **49**, 1768–1777.

**Umebayashi T, Utsumi Y, Koga S, Murata I, Fukuda K.** 2016. Differences in drought- and freeze-induced embolisms in deciduous ring-porous plant species in Japan. *Planta* **244**, 753–760.

**Van As H.** 2007. Intact plant MRI for the study of cell water relations, membrane permeability, cell-to-cell and long distance water transport. *Journal of Experimental Botany* **58**, 743–756.

**Van As H, Scheenen T, Vergeldt FJ.** 2009. MRI of intact plants. *Photosynthesis Research* **102**, 213–222.

**Van As H, van Duynhoven J.** 2013. MRI of plants and foods. *Journal of Magnetic Resonance* **229**, 25–34.

**van Dusschoten D, Metzner R, Kochs J, Postma JA, Pflugfelder D, Bühler J, Schurr U, Jahnke S.** 2016. Quantitative 3D analysis of plant roots growing in soil using magnetic resonance imaging. *Plant Physiology* **170**, 1176–1188.

**Van Norman JM.** 2015. Root system patterning: auxin synthesis at the root periphery. *Current Biology* **25**, R460–R462.

**Weber T, Ziener CH, Kampf T, Herold V, Bauer WR, Jakob PM.** 2009. Measurement of apparent cell radii using a multiple wave vector diffusion experiment. *Magnetic Resonance in Medicine* **61**, 1001–1006.

**Wesbey GE, Moseley ME, Ehman RL.** 1984. Translational molecular self-diffusion in magnetic resonance imaging. II. Measurement of the self-diffusion coefficient. *Investigative Radiology* **19**, 491–498.

**Windt CW, Blümler P.** 2015. A portable NMR sensor to measure dynamic changes in the amount of water in living stems or fruit and its potential to measure sap flow. *Tree Physiology* **35**, 366–375.

**Windt CW, Gerkema E, Van As H.** 2009. Most water in the tomato truss is imported through the xylem, not the phloem: a nuclear magnetic resonance flow imaging study. *Plant Physiology* **151**, 830–842.

**Xu M, Zhu L, Shou H, Wu P.** 2005. A *PIN1* family gene, *OsPIN1*, involved in auxin-dependent adventitious root emergence and tillering in rice. *Plant & Cell Physiology* **46**, 1674–1681.